symmetry

MDPI

Article

Room Temperature Syntheses of ZnO and Their Structures

Domenica Tommasa Donia [1], Elvira Maria Bauer [2], Mauro Missori [3], Ludovica Roselli [4], Daniele Cecchetti [4], Pietro Tagliatesta [4], Lorenzo Gontrani [5,*] and Marilena Carbone [2,4,*]

1 Department of Surgical Science, University of Rome Tor Vergata, Via Montpellier 1, 00133 Rome, Italy; donia@med.uniroma2.it
2 Italian National Research Counci—Institute of Structure of Matter (CNR-ISM), Via Salaria km 29.3, 00015 Monterotondo, Italy; elvira.bauer@ism.cnr.it
3 Institute of Complex Systems, National Research Council (CNR-ISC) and Department of Physics, Sapienza University of Rome, 00185 Rome, Italy; mauro.missori@isc.cnr.it
4 Department of Chemical Science and Technologies, University of Rome Tor Vergata, Via della Ricerca Scientifica 1, 00133 Rome, Italy; ludoroselli@virgilio.it (L.R.); daniele.gena@gmail.com (D.C.); pietro.tagliatesta@uniroma2.it (P.T.)
5 Department of Chemistry, Sapienza University of Rome, P.le A. Moro 2, 00185 Rome, Italy
* Correspondence: Lorenzo.Gontrani@uniroma1.it (L.G.); Carbone@uniroma2.it (M.C.)

Abstract: ZnO has many technological applications which largely depend on its properties, which can be tuned by controlled synthesis. Ideally, the most convenient ZnO synthesis is carried out at room temperature in an aqueous solvent. However, the correct temperature values are often loosely defined. In the current paper, we performed the synthesis of ZnO in an aqueous solvent by varying the reaction and drying temperatures by 10 °C steps, and we monitored the synthesis products primarily by XRD). We found out that a simple direct synthesis of ZnO, without additional surfactant, pumping, or freezing, required both a reaction (T_P) and a drying (T_D) temperature of 40 °C. Higher temperatures also afforded ZnO, but lowering any of the T_P or T_D below the threshold value resulted either in the achievement of $Zn(OH)_2$ or a mixture of $Zn(OH)_2$/ZnO. A more detailed Rietveld analysis of the ZnO samples revealed a density variation of about 4% (5.44 to 5.68 gcm^{-3}) with the synthesis temperature, and an increase of the nanoparticles' average size, which was also verified by SEM images. The average size of the ZnO synthesized at $T_P = T_D = 40$ °C was 42 nm, as estimated by XRD, and 53 ± 10 nm, as estimated by SEM. For higher synthesis temperatures, they vary between 76 nm and 71 nm (XRD estimate) or 65 ± 12 nm and 69 ± 11 nm (SEM estimate) for $T_P = 50$ °C, $T_D = 40$ °C, or $T_P = T_D = 60$ °C, respectively. At $T_P = T_D = 30$ °C, micrometric structures aggregated in foils are obtained, which segregate nanoparticles of ZnO if T_D is raised to 40 °C. The optical properties of ZnO obtained by UV-Vis reflectance spectroscopy indicate a red shift of the band gap by ~0.1 eV.

Keywords: ZnO; room temperature synthesis; XRD characterization; SEM morphology; UV-Vis reflectance spectroscopy

Citation: Donia, D.T.; Bauer, E.M.; Missori, M.; Roselli, L.; Cecchetti, D.; Tagliatesta, P.; Gontrani, L.; Carbone, M. Room Temperature Syntheses of ZnO and Their Structures. *Symmetry* **2021**, *13*, 733. https://doi.org/10.3390/sym13040733

Academic Editor: Jesús F. Arteaga

Received: 24 March 2021
Accepted: 13 April 2021
Published: 20 April 2021

1. Introduction

Metal and mixed metal and semiconductor oxides are widely applied in several fields, as supercapacitors [1–3], gas sensors based on chemoresistivity [4–8] or dielectric excitation [9,10], heterojunctions [11,12], energy storage in batteries [13–15], and electrochemistry [16–18]. Their properties can be varied in different ways, by doping [19,20], capping, and controlling the structure, shape, and size with bottom-up and top- down approaches [21–28]. The types of synthesis include sol-gel methods, hydrothermal synthesis, solvothermal synthesis, and electrospinning [29–35]. Among the oxides, ZnO has been thoroughly investigated because of its properties, such as a wide band gap (~3.35 eV) with a high exciton binding energy of (~60 meV), wurtzite crystal structure, piezoelectric properties, and relatively low cost [36,37], which make it a suitable candidate for energy

conversion/storage, high-performance electronics, photocatalysis, sensors, solar cells, and supercapacitors [38–42]. In addition, it is applied in environmental remediation [43,44], as a biocide, and as a nanofertilizer in agriculture [45,46].

The synthetic strategy and the careful control of the synthesis parameters play a key role in determining ZnO's properties. Environmentally-friendly syntheses must be privileged, on account of the extent of ZnO applications and the consequent sizeability of its production. Ideally, a green synthesis is performed at room temperature with water solvent, and possibly a high yield. In this framework, we reviewed the literature in search of the optimum synthesis conditions. However, when exploring RT syntheses, it appeared that quite a large variety of parameters are included under the RT label, or that additional operations besides RT synthesis are required to achieve pure ZnO.

A common feature to all syntheses is the use of a large excess of base, typically NaOH, with respect to the Zn salt ($Zn(NO_3)_2$, $Zn(CH_3CO_2)_2$), from a minimum of five and up to 50 times larger. Room temperature synthesis was carried out at 25 °C, with double jet conditions, controlling the shape and size of the ZnO by the pH of the solution (pH 9.5 to 10.5). In addition, a surfactant (sodium dodecyl sulfate) was used. Following operations required the precipitate to be washed with distilled water, frozen, and subsequently vacuum dried [47].

A synthesis was carried out at RT (exact value not specified) [48] by keeping the solution sealed and in the dark for up to 60 days, centrifuging, washing with water and ethanol, and then drying under vacuum. The XRD patterns indicated the formation of ZnO, although spectra were reported starting from $2\theta > 20^\circ$, whereas the signature reflexes of $Zn(OH)_2$ appeared very near that boundary ($2\theta = 20.16^\circ$ and $2\theta = 20.89^\circ$) [49]. A synthesis of ZnO nanoparticles as well as micrometric agglomerates was performed at RT by using $Zn(CH_3CO_2)_2$ and a mixture of NaOH and NH_4F in a water solution in variable proportions. The reaction was carried out for 10 min, followed by centrifugation, washing with water and ethanol, and drying at temperatures between 60 °C and 75 °C [50]. Sonochemistry was used for 10 min in the RT synthesis, followed by 2–4 h sonication at 40 KHz, filtration, washing with methanol, and drying at RT [51]. In this case, the sonication procedure could be crucial, not only because of the ultrasound waves sent to the sample, but also for the temperature of the bath, which tends to increase during the sonication if it is not externally controlled. Syntheses at different temperatures by 10 °C stepwise, increasing between 0 °C and 80 °C, were carried out from $Zn(CH_3CO_2)_2$ and NaOH water solutions, followed by centrifugation and washing with water. In this case, the drying was achieved by lyophilization [52]. In all cases, ZnO was reported as the sole product, though the XRD patterns started off at $2\theta = 20^\circ$, and significant $Zn(OH)_2$ contributions were excluded. In a relatively quick synthetic procedure, ZnO was achieved at RT by precipitation, 30 min stirring, and 1 h ageing. However, the drying followed at 60 °C, though the length of the latter is not mentioned [53].

A synthesis at RT was reported by Kumar et al. [54], in which NH_4OH was added dropwise to a water solution of $Zn(NO_3)_2$ of unspecified concentration under controlled, though not disclosed, pH, followed by 48 h RT drying.

All-in-all, ZnO is either not fully achieved by carrying out operations solely at room temperature, or insufficient details are reported, or, simply, it is not always clear what the room temperature was during the synthetic procedure.

In the current paper, we explore the effects of 'room temperature' on the achievement of ZnO and on its structure by carrying out syntheses in water and controlling reaction and drying temperatures in steps of 10 °C.

The aim is to find the conditions for synthesizing pure ZnO at temperatures as close as possible to the textbook definition of room temperature—i.e., 25 °C—with a procedure as simple as possible, by precipitation from water solutions, with the sole use of reacting salts, hence without surfactants, and with the minimum number of operations, thus without pumping and/or freezing.

Under these conditions the minimum temperature for synthesizing pure ZnO nanoparticles is 40 °C, for both phases (reaction and drying), whereas at 30 °C, only $Zn(OH)_2$ is achieved. At higher synthesis temperatures, ZnO is also obtained, though of a larger average size and slightly different volume, density, and cell parameters. In particular, the density experiences a 4% increase by increasing the synthesis temperature from 5.44 g cm^{-3} (sample achieved and dried at 40 °C) to 5.68 g cm^{-3} (sample achieved at 50 °C and dried at 40 °C), whereas it decreases to 5.61 g cm^{-3} if the drying temperature is raised. The corresponding average sizes of the crystallites (estimated by XRD) are 42 nm, 76 nm, and 71 nm, respectively. Comparatively, the average sizes estimated by SEM are 53 ± 10 nm, 65 ± 12 nm and 69 ± 11 nm, respectively. The band gap of ZnO is consistent with the nanoparticle nature of the synthesized samples, and shows a red shift to 3.25–3.26 eV (as compared 3.35–3.36 eV of bulk ZnO). The size calculated through the optical measurements is ~15 nm, and indicates the smallest dimension of anisotropic particles as the minimum pathway of an electronic transition through a gap.

2. Materials and Methods

All of the chemicals were of reagent grade, and were used without any further purification. $Zn(NO_3)_2$, and NaOH were purchased from Sigma-Aldrich. All of the solutions were prepared with deionized water.

The syntheses were carried out according to the following reaction:

$$Zn(NO_3)_2 + 2NaOH \xrightarrow{T_P} Zn(OH)_{2(s)}\ ,\ ZnO_{(s)} + 2NaNO_{3(aq)} \xrightarrow{T_D} ZnO_{(s)} + H_2O + 2NaNO_{3(aq)} \quad (1)$$

where T_P is the temperature of the precipitation reaction and T_D is the drying temperature. More in detail, a 0.1 M $Zn(NO_3)_2$ solution was first prepared in deionized water, and was stirred for a few minutes until complete dissolution. Then, an equal volume of a 0.1 M NaOH solution was added dropwise to the solution kept constant in an oil bath at the selected temperature and stirred for 24 h.

In the first instance, in the selection of the synthesis parameters, the ratio between $Zn(NO_3)_2$ and NaOH was kept at 1:1, i.e., in excess of Zn^{2+}. This implies an initial pH of 6, which corresponds to the minimum of ZnO solubility in water (at 25 °C) [55], in order to ensure that the formed ZnO does not redissolve. In a typical synthesis, the reaction is carried out at a given temperature (T_P), the slurry is digested for two hours, centrifuged (3500 rpm for 10 min), washed with distilled water multiple times, and then dried at the chosen temperature (T_D) in an oven for 72 h. A white powder is then achieved, which is further characterized. The summary of the syntheses conditions is reported in Table 1.

Table 1. Samples' preparation conditions.

Sample	Reaction Temperature	Drying Temperature
P30D30	30 °C	30 °C
P30D40	30 °C	40 °C
P40D40	40 °C	40 °C
P50D30	50 °C	30 °C
P50D50	50 °C	50 °C
P60D60	60 °C	60 °C

The X-ray diffraction (XRD) patterns of the synthesized samples were collected with an X'pert pro X-ray diffractometer by Philips, using CuK-Alpha radiation. They were then analyzed by a Rietveld procedure with the GSAS-II suite of programs [56]. The Rietveld fitting refines the peak intensities and crystal cell edges (Å), and consequently the volume ($Å^3$) and density (g cm^{-3}) of the phase, as well as the relative amount of the phases in the case of mixtures. It also yields the average value of the crystallites size τ, according to the Scherrer equation $\tau = k\lambda/\beta\cos(\theta)$, where β is the line broadening at half the maximum intensity (FWHM), λ is the radiation wavelength (1.54 Å), θ is the Bragg angle, and the

shape factor k used was 0.9. Scanning Electron micrographs (SEMs) were collected with a Zeiss Auriga 405 Field Emission-Scanning Electron Microscope instrument, mounting a Gemini column and operating at 7 kV.

Optical measurements in the ultraviolet (UV), visible (Vis), and near infrared (NIR) spectral regions were obtained by a diffuse reflectance setup from Avantes BV (The Netherlands). The latter comprises a combined deuterium–halogen radiation source (AvaLight-DH-S-BAL) connected via an optical fiber to a 30 mm-diameter Spectralon® coated integrating sphere (an AvaSphere-30-REFL was used to illuminate the samples (sampling port diameter 6 mm)), and it collects the radiation diffusely reflected from all angles. The ZnO powders were placed in the well of a sample holder with a depth such as to be able to consider the reflectance spectra as those of an infinitely thick sample (R_∞). The integrating sphere was connected through another optical fiber to a spectrometer (AvaSpec-2048 × 14-USB2). This configuration allows applications in the 248–1050 nm range with a 2.4 nm spectral resolution. A laptop was used for the spectrometer control and data recording, whereas a factory-calibrated Spectralon® (Labsphere, USA) was used as the reflectance reference. Each reflectance spectrum was obtained by averaging 5 acquisitions lasting 5 s each.

3. Results and Discussion

The synthesis of ZnO can be depicted as a two-stages process, i.e., precipitation and drying. The achievement of the ZnO, rather than $Zn(OH)_2$ or a combination of the two moieties, strictly depends on the operational modalities of the two stages.

In the present paper, we opted to determine the best match in terms of the temperature of each of the two steps, aiming to find the lowest possible ones which would guarantee no detectable presence of $Zn(OH)_2$. In this framework, the drying temperature plays a role in the achievement of ZnO, as it allows the dehydration of residual $Zn(OH)_2$ from the precipitation step. The verification of the composition was primarily carried out by XRD. Additional information on the fine structure of ZnO was determined by Rietveld refinement. A first synthesis was carried out at $T_P = T_D = 30$ °C, and was hence the closest, in our experimental setup, to the classical definition of RT = 25 °C. In this setup, we obtained nearly 100% $Zn(OH)_2$ samples (Figure 1). We then increased the drying temperature by 10 °C in order to achieve the sample P30D40, and subsequently increased the reaction temperature by 10 °C (sample P40D40). The former setup still affords a mixture of ZnO and $Zn(OH)_2$, whereas the XRD of the latter indicates the sole presence of ZnO. We also verified that a temperature of 40 °C was strictly necessary to achieve ZnO by varying the reaction temperature to 50 °C and using either 30 °C or 40 °C for the drying procedure. Once more, the former yielded a mixture of ZnO and $Zn(OH)_2$, whereas the latter was pure ZnO. Finally, we performed a synthesis at $T_P = T_D = 60$ °C, obtaining pure ZnO. Therefore, in general, 40 °C is the threshold temperature necessary both for the reaction and for drying in order to achieve ZnO.

As the RT ZnO syntheses reported in the literature are typically carried out in basic conditions, with a $Zn(NO_3)_2$:NaOH ratio of 1:5 to 1:50 [52–59] and pH $\geq$ 12, we verified whether basic conditions would allow lower temperature conditions, and carried out a synthesis using a $Zn(NO_3)_2$:NaOH ratio of 1:10, at $T_P = T_D = 30$ °C. In the latter case, we only achieved $Zn(OH)_2$ (XRD not shown).

The powder X-Ray diffraction spectra of all of the samples—P30D30, P30D40, P40D40, P50D30, P50D40 and P60D60—were first visually compared (Figure 1) and then analyzed with Rietveld refinement using the GSAS-II software [56]. P40D40, P50D40 and P60D60 proved to be composed of pure ZnO, and the difference of the structural parameters was investigated, whereas P30D30, P30D40, and P50D30, on the contrary, turned out to contain both the target product (ZnO) and the precursor $Zn(OH)_2$. For this reason, the relative composition of the two solid phases in the mixture was assessed in addition to the structural parameters. The preliminary qualitative comparison of the spectra pointed out that in P60D60, P50D40, and P40D40—the peak positions are similar; the only notable

difference being their intensity, which was highest for P60D60 and comparable in the other two systems. A common crystal structure can therefore be envisaged for them. A more accurate analysis, though (see Figure 2), shows that the most intense peaks from P60D60 fall almost in the middle between the P40D40 peaks (lower angle) and P50D40 ones (higher angle). The latter two sets of peaks are shifted by 0.1 degrees, on average.

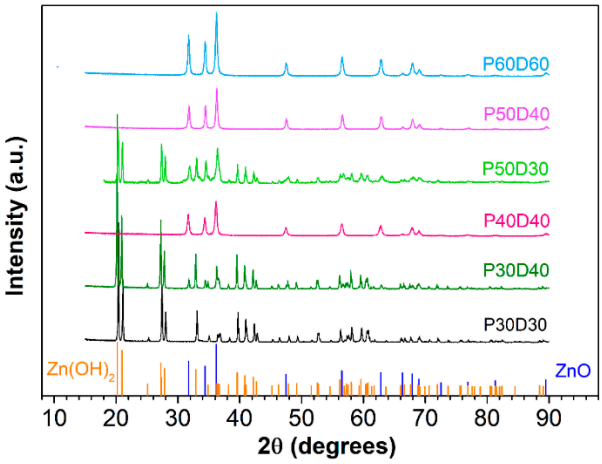

Figure 1. XRD patterns of the synthesized samples.

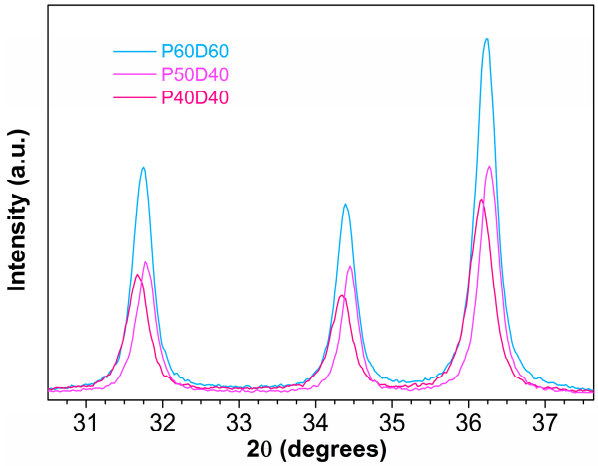

Figure 2. Details of the XRD patterns of pure zinc oxide samples.

This issue suggests that a slight change of some crystal parameter(s) occurs among the three structures. Regarding P30D40, P30D30, and P50D30, the patterns are characterized by a large number of new peaks that show up in all of the angle ranges, especially the very intense ones before 30 degrees, a portion of the spectrum where no peaks are found in P60D60, P50D40 and P40D40. The crystal structures of the mineral zincite (100% ZnO, space group P63mc) [57] and of Wulfingite (pure zinc hydroxide, P212121) [48] were then employed in the fitting procedure. The single-crystal phase data were downloaded from the American Mineralogist Crystal Structure Database [58] as Crystallographic Information Files (CIF). The simulated powder pattern for each sample was obtained for CuK_α wavelength (1.54 Å), modelling the peak shapes with a convolution of modified asymmetric pseudo-Voigt functions [59]. The background was modelled with a three-term Chebyshev polynomial of the first kind. The P60D60 profile was successfully fitted on 3100 observations, reaching the weighted-profile R factor wR = 11.76%, R = 8.20%, χ^2 = 5420.14 at convergence. The same approach was adopted for the other systems, obtaining wR = 14.96%, R = 10.83%, χ^2 = 6382.69 for P50D40; wR = 14.16%, R = 9.79%, χ^2 = 5254.82 for P40D40; wR = 24.82%, R = 17.94%, and χ^2 = 3188.23 for P30D40; wR = 17.36 %, R= 13.09 %, χ^2 = 15145.9 for

P30D30; and wR = 24.82%, R = 17.94% and χ^2 = 3188.23 for P50D30. The ratio between the oxide and hydroxide phase fractions in the mixtures was fitted as well, obtaining the following ZnO:$Zn(OH)_2$ ratios: 22:78, 0.05:99.5 and 69:31 for P30D40, P30D30, and P50D30, respectively. The fitting plots are reported in the Supplementary Information Figures S1–S6. The sample P30D30 will be, from now on, considered as pure hydroxide for simplicity. The fitting procedure also returns the optimized structural parameters for the cell(s) and the atom positions; the additional fitted parameters were the domain size and microstrain of the crystallites, as well as the sample position and the instrumental broadening parameters U, V, and W. The most important parameters are reported in the tables below (Table 2 for pure ZnO, Table 3 for the mixtures); the reference to the corresponding fitting plot in the Supplementary Information for each system is given in the table caption.

Table 2. Pure ZnO systems. Fitted cell parameters, crystallite sizes and fractional coordinates. The fitting plots are reported in Figure S3 (P40D40), Figure S5 (P50D40), and Figure S6 (P60D60).

Sample	a (Å)	b (Å)	c (Å)	Volume (Å^3)	Density (gcm^{-3})	Cryst. Size (nm)
P40D40	3.32	3.32	5.22	49.70	5.44	42
P50D40	3.25	3.25	5.21	47.56	5.68	76
P60D60	3.27	3.27	5.21	48.17	5.58	71
Fractional Coordinates	**X (Zn)**	**Y (Zn)**	**Z (Zn)**	**X (O)**	**Y (O)**	**Z (O)**
P40D40	0.33	0.67	−0.23	0.33	0.67	0.37
P50D40	0.33	0.67	−0.05	0.33	0.67	0.35
P60D60	0.33	0.67	−0.02	0.33	0.67	0.37

Table 3. Mixed ZnO/$Zn(OH)_2$ systems. Fitted cell parameters, crystallite sizes, and fractional coordinates. The fitting plots are reported in Figure S2 (P30D40), Figure S1 (P30D30), and Figure S4 (P50D30).

Sample/Phase	a (Å)	b (Å)	c (Å)	Volume (Å^3)	Density (gcm^{-3})	Cryst. Size (nm)	Fraction		
P30D40									
ZnO	3.26	3.26	5.21	47.88	5.65	90	22.46%		
$Zn(OH)_2$	4.91	5.14	8.47	213.84	3.09	243	77.54%		
Fractional Coordinates	**X(Zn)**	**Y (Zn)**	**Z (Zn)**	**X(O1)**	**Y (O1)**	**Z (O1)**	**X(O2)**	**Y (O2)**	**Z (O2)**
ZnO	0.33	0.67	−0.02	0.33	0.67	0.36			
$Zn(OH)_2$	0.07	0.65	0.62	0.13	0.13	0.08	0.19	0.31	0.73
Sample/Phase	**a (Å)**	**b (Å)**	**c (Å)**	**Volume (Å^3)**	**Density (gcm^{-3})**	**Dom. Size (nm)**	**Fraction**		
P30D30									
$Zn(OH)_2$	4.67	5.46	8.36	212.99	3.10	261	≈100%		
Fractional Coordinates	**X(Zn)**	**Y (Zn)**	**Z (Zn)**	**X(O1)**	**Y (O1)**	**Z (O1)**	**X(O2)**	**Y (O2)**	**Z (O2)**
$Zn(OH)_2$	0.07	0.65	0.62	0.11	0.13	0.08	0.19	0.31	0.73
Sample/Phase	**a (Å)**	**b (Å)**	**c (Å)**	**Volume (Å^3)**	**Density (gcm^{-3})**	**Dom. Size (nm)**	**Fraction**		
P50D30									
ZnO	3.24	3.24	5.20	47.45	5.70	36	68.98%		
$Zn(OH)_2$	4.90	5.13	8.46	212.56	3.11	900	31.02%		
Fractional Coordinates	**X(Zn)**	**Y (Zn)**	**Z (Zn)**	**X(O1)**	**Y (O1)**	**Z (O1)**	**X(O2)**	**Y (O2)**	**Z (O2)**
ZnO	0.33	0.67	−0.02	0.33	0.67	0.37			
$Zn(OH)_2$	0.07	0.64	0.63	0.13	0.12	0.09	0.16	0.36	0.72

An interesting feature which was pointed out during the refinement was the difference in the cell parameters of the three pure zinc oxide samples. The cell parameter refinement

confirmed that P60D60 has an intermediate behavior with respect to P50D40 and P40D40. The cell dimensions and the resulting volume (and density) fall in the middle of the range, in compliance with the peak positions already discussed above. The density order P40D40 < P60D60 < P50D40 is nicely anticorrelated with the position of the peaks, i.e., P50D40; the densest structure—having structural correlations that occur at smaller distance on average—gives origin to diffraction peaks that fall at larger angles (according to the scattering vector and Bragg's law definitions $q = 4\pi \sin\theta/\lambda$ and $d = 2\pi/q$ [60,61]), while the distances between the atoms contained in the least dense sample (P40D40) are typically larger, and the resulting peaks fall at smaller angle. Interestingly, the cell dimensions are larger when the average dimension of the crystallites is smaller. When compared with the single-crystal cell dimensions (a = 3.2495 c = 5.2069, values in Å), or with some recently reported ZnO nanosheets (a = 3.245 c = 5.198, [53]), the first nanoparticle sample (P40D40) appears to be significantly less dense, while the calculated density values for the other two systems are closer, and satisfactorily comply with the bulk experimental density value of 5.61 g cm^{-3} [62]. The modulation of the structural features observed demonstrates that our synthesis protocol—by a simple tuning of the temperature—is capable of leading, easily and successfully, to final products with different properties.

The synthesized samples display different types of morphology, depending on the temperature adopted in the different phases of the synthesis. Examples of the morphology of the samples are reported in Figure 3. The P30D30 sample, mostly composed of $Zn(OH)_2$, has a micrometric structure of aggregated foils. In the P30D40 sample, the micrometric arrangements become more compact to form blocks, and some nanoparticles appear on their surface, as is highlighted in Figure 3b with light orange circles. Once pure ZnO is formed, i.e., when both the reaction and drying temperatures are, at least, 40 °C, the samples are characterized by the shear presence of nanoparticles. The nanoparticle morphology of ZnO is retained for higher synthesis temperatures, though the average size is slightly larger. In particular, the average size of the P40D40, P50D40 and P60D60 are 53 ± 10 nm, 65 ± 12 nm and 69 ± 11 nm, respectively, and are thus in agreement with the crystallite size detected by XRD within the experimental error (Tables 2 and 3). In addition, there is a good agreement between the estimated crystallite size and the samples' morphologies for mixed $Zn(OH)_2$/ZnO samples with larger average sizes associated to $Zn(OH)_2$ as compared to ZnO. XRD allows a separate assessment of the average size of each phase. Though this is not possible by SEM imagining, as the morphology cannot quite distinguish the crystallographic phase, it can be hypothesized that the small nanoparticles on the surface of the blocks in the P30D40 sample are actually ZnO deriving from the $Zn(OH)_2$ dehydration.

The band gap of the ZnO nanoparticles samples was estimated by diffuse reflectance R_∞ spectra, where R_∞ is the reflectance of an infinitely thick layer of the sample, converted into absorption spectra by using the Kubelka–Munk function [63,64]:

$$\frac{K}{S} \equiv \frac{(1 - R_\infty)^2}{2R_\infty} \tag{2}$$

where K and S are the Kubelka–Munk absorption and scattering coefficients, respectively. The K absorption coefficient is related to the intrinsic absorption coefficient of the particles α by $\alpha = K/2$, in the case of diffuse light distribution, as in our case [65]. The steady preparation of ZnO powder samples for optical measurements also allowed us to consider S to be constant from sample to sample; then, the ratio $K/S \approx \alpha$. In order to estimate the band gap from the absorption spectra, we can then apply the Tauc relation [66]:

$$\alpha h\upsilon = C1\left(h\upsilon - E_g\right)^n \tag{3}$$

where $n = 1/2$ for the indirect gap and $n = 2$ for direct gaps, such as for the case of ZnO, and C1 is a constant (Figure 4).

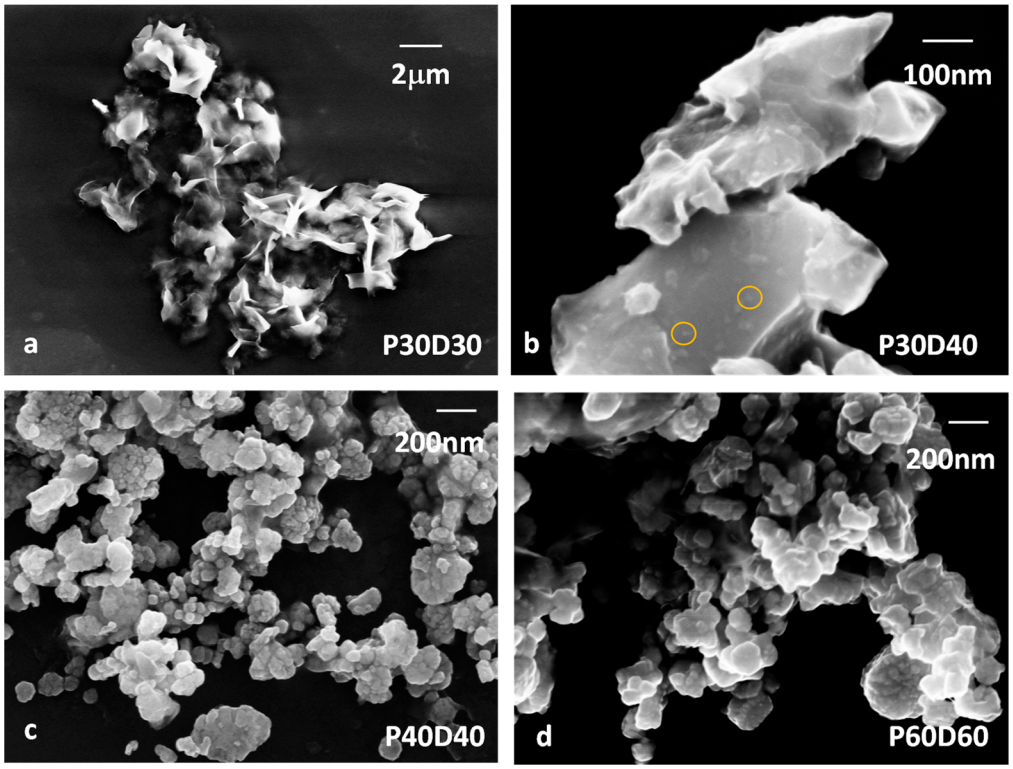

Figure 3. Selected SEM images of the synthesized samples: (**a**) P30D30, (**b**) P30D40, (**c**) P40D40, and (**d**) P60D60.

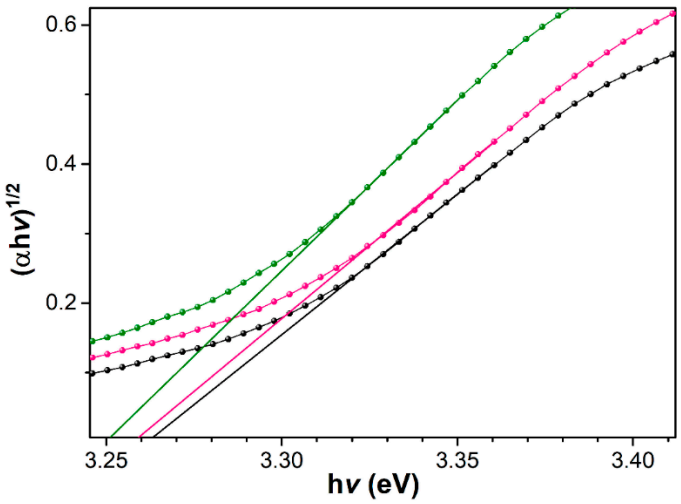

Figure 4. Tauc plots for the determination of the optical band gap E_g (lines + dots) and associated extrapolations of the linear regions (solid lines). Green corresponds to the sample P40D40, red to P50D40 and black to P60D60.

The ZnO band gap E_g, including the quantum confinement as a function of the average particle size, is obtained from the effective mass model given by [67,68]:

$$E_g \cong E_g^{bulk} + \frac{h^2}{8e\mu r^2} - \frac{1.8e}{4\pi\varepsilon_r\varepsilon_0 r} - \frac{0.124e^3\mu}{(2h\varepsilon_r\varepsilon_0)^2} \quad (4)$$

In this equation, all of the terms are in eV: E_g^{bulk} is the bulk ZnO band gap (3.35 eV), h is the Planck constant, r is the particle radius, e is the charge of the electron, and μ is the

reduced mass of the electron and holes $\mu = \frac{m_e^* m_h^*}{m_e^* + m_h^*}$, where m_e^* and m_h^* are the effective mass of the electrons and holes in ZnO, respectively, $m_e^* = 0.19 m_e$ and $m_h^* = 0.8 m_e$, where m_e is the free electron mass [69]; ε_r (3.7) is the relative permittivity, and ε_0 is the permittivity of the free space.

The *Eg* values of 3.25 (0), 3.25 (8), and 3.26 (2) eV (Table 4) injected in the previous equation all yield nanoparticles sizes (2*r*) of about 15 nm, providing an estimation of the smaller size in the synthesized ZnO nanoparticles.

Table 4. Band gap of the ZnO samples.

Sample	Band Gap (eV)
P40D40	3.25 (0)
P50D40	3.25 (8)
P60D60	3.26 (2)

Compared to a band gap of 3.35 eV in bulk ZnO [70], P40D40, P50D40, P60D60 exhibit a red shift by ~0.1 eV. ZnO nanoparticles, in general, may undergo both a blue and a red shift, with many factors concurring to the actual band gap value. As shown by Equation (1), below a 14 nm diameter threshold, the size effect is dominant and a blue shift is observed [71,72]. However, the shape also plays a role and both red and blue shift were observed, depending on the particles morphology, as determined by the employment of different solvents during the synthesis [73]. In RT synthesis followed by lyophilization, a red shift by ~0.1 eV has been observed between synthesis at 20 °C and at 50 °C, and it has been associated to a slight size increase of the nanoparticles [52]. However, a simultaneous shape change was also observed from elliptical to conical, which may contribute to the red shift. P40D40, P50D40, P60D60 have similar morphologies, and the comparable band gap values would indicate similar average sizes. A comparison with the XRD results, which give domain sizes ranging from 42 to 76 nm, suggests a shape anisotropy for the P40D40, P50D40, and P60D60 nanoparticles, which can be also observed from the SEM images (Figure 3c,d). It must be added that the average particle size in the band gap corresponds to the pathway for an electronic transition through a gap, which can be equivalent for anisotropic samples with similar minimum size pathways.

4. Conclusions

Our studies evidence that room temperature synthesis of ZnO nanoparticles by precipitation from an aqueous solution is possible, provided that the exact temperature parameters are carefully selected. We found that the reaction and drying temperatures are equally important, and they need to be at least 40 °C in order to provide pure ZnO. A lower temperature for any of the two synthetic phases results in a mixture of $ZnO/Zn(OH)_2$, or in the synthesis of $Zn(OH)_2$. The morphology is similar for all ZnO nanoparticles, as well as for the optical band gap. However, the size of the ZnO nanoparticles is also temperature dependent, and it is smaller for lower temperatures. The morphology of the lower-temperature samples ($Zn(OH)_2$) indicated the presence of aggregated foils, which merge to form blocks, from which ZnO nanoparticles eventually detach. The results obtained from the SEM experiments comply quite well with the X-Ray diffraction experiments and the optical analysis of the band gap, where it was found that the scattering patterns observed for the samples synthesized at temperatures greater than 40 °C show a shape anisotropy and an evident shift towards smaller angles, thus indicating systems of larger average dimensions and crystallite sizes.

Supplementary Materials: The following are available online at https://www.mdpi.com/article/10.3390/sym13040733/s1. Figures S1 through S6: XRD patterns of the samples P30D30, P30D40, P40D40, P50D30, P50D40, P60D60 and associated Rietveld fits.

Author Contributions: Conceptualization, M.C. and D.T.D.; methodology, D.T.D., M.M.; software, M.M., L.R.; validation, L.R., D.T.D., M.M.; formal analysis, E.M.B.; investigation, D.T.D., L.R., M.M., E.M.B.; resources, M.C.; data curation, D.C., P.T.; writing—original draft preparation, M.C., L.G.; writing—review and editing, M.C., L.G.; supervision, M.C.; project administration, M.C. All authors have read and agreed to the published version of the manuscript.

Funding: This research received no external funding.

Informed Consent Statement: Not applicable.

Data Availability Statement: The data presented in this study are contained within the article or supplementary material.

Acknowledgments: The authors thank F. Mura from CNIS (Sapienza University of Rome) for his contribution to the SEM characterization of the images.

Conflicts of Interest: The authors declare no conflict of interest.

References

1. Keimer, B.; Kivelson, S.A.; Norman, M.R.; Uchida, S.; Zaanen, J. From Quantum Matter to High-temperature Superconductivity in Copper Oxides. *Nature* **2015**, *518*, 179–186. [CrossRef]
2. Rijckaert, H.; Pollefeyt, G.; Sieger, M.; Hänisch, J.; Bennewitz, J.; De Keukeleere, K.; De Roo, J.; Hühne, R.; Bäcker, M.; Paturi, P.; et al. Optimizing Nanocomposites through Nanocrystal Surface Chemistry: Superconducting $YBa_2Cu_3O_7$ Thin Films via Low-Fluorine Metal Organic Deposition and Preformed Metal Oxide Nanocrystals. *Chem. Mater.* **2017**, *29*, 6104–6113. [CrossRef]
3. Chakhalian, J.; Liu, X.; Fiete, G.A. Strongly Correlated and Topological States in Grown Transition Metal Oxide Thin Films and Heterostructures Editors-pick. *APL Mater.* **2020**, *8*, 050904. [CrossRef]
4. Neri, G. First Fifty Years of Chemoresistive Gas Sensors. *Chemosensors* **2015**, *3*, 1–20. [CrossRef]
5. Carbone, M. CQDs@NiO: An Efficient Tool for CH_4 Sensing. *Appl. Sci.* **2020**, *10*, 6251. [CrossRef]
6. Sturaro, M.; Della Gaspera, E.; Michieli, N.; Cantalini, C.; Emamjomeh, S.M.; Guglielmi, M.; Martucci, A. Degenerately Doped Metal Oxide Nanocrystals as Plasmonic and Chemoresistive Gas Sensors. *ACS Appl. Mater. Interfaces* **2016**, *8*, 30440–30448. [CrossRef]
7. Lin, T.; Lv, X.; Hu, Z.; Xu, A.; Feng, C. Semiconductor Metal Oxides as Chemoresistive Sensors for Detecting Volatile Organic Compounds. *Sensors* **2019**, *19*, 233. [CrossRef] [PubMed]
8. Carbone, M.; Tagliatesta, P. NiO Grained-flowers and Nanoparticles for Ethanol Sensing. *Materials* **2020**, *13*, 1880. [CrossRef]
9. Potyrailo, R.A.; Go, S.; Sexton, D.; Li, X.; Alkadi, N.; Kolmakov, A.; Amm, B.; St-Pierre, R.; Scherer, B.; Nayeri, M.; et al. Extraordinary Performance of Semiconducting Metal Oxide Gas Sensors Using Dielectric Excitation. *Nat. Electron.* **2020**, *3*, 80–289. [CrossRef]
10. Lee, H.J. Linear Gas Sensing with Dielectric Excitation. *Nat. Electron.* **2020**, *3*, 239–240. [CrossRef]
11. Yao, Y.; Sang, D.; Duan, S.; Wang, Q.; Liu, C. Review on the Properties of Boron-Doped Diamond and One-Dimensional-Metal-Oxide Based P-N Heterojunction. *Molecules* **2021**, *26*, 71. [CrossRef]
12. Staerz, A.; Gao, X.; Cetmi, F.; Ming, Z.; Weimar, U.; Zhang, T.; Barsan, N. Dominant Role of Heterojunctions in Gas Sensing with Composite Materials. *ACS Appl. Mater. Interfaces* **2020**, *12*, 21127–21132. [CrossRef] [PubMed]
13. Carbone, M. Zn Defective $ZnCo_2O_4$ Nanorods as High Capacity Anode for Lithium Ion Batteries. *J. Electroanal. Chem.* **2018**, *815*, 151–157. [CrossRef]
14. Fang, S.; Bresser, D.; Passerini, S. Transition Metal Oxide Anodes for Electrochemical Energy Storage in Lithium- and Sodium-Ion Batteries. *Adv. Energy Mater.* **2020**, *10*, 1902485. [CrossRef]
15. Li, Q.; Li, H.; Xia, Q.; Hu, Z.; Zhu, Y.; Yan, S.; Ge, C.; Zhang, Q.; Wang, X.; Shang, X.; et al. Extra Storage Capacity in Transition Metal Oxide Lithium-ion Batteries Revealed by in situ Magnetometry. *Nat. Mater.* **2021**, *20*, 76–83. [CrossRef]
16. Carbone, M.; Nesticò, A.; Bellucci, N.; Micheli, L.; Palleschi, G. Enhanced Performances of Sensors Based on Screen Printed Electrodes Modified with Nanosized NiO Particles. *Electrochim. Acta* **2017**, *246*, 580–587. [CrossRef]
17. Agnihotri, A.S.; Varghese, A.; Nidhin, M. Transition Metal Oxides in Electrochemical and Bio Sensing: A State-of-art Review. *Appl. Surf. Sci. Adv.* **2021**, *4*, 100072. [CrossRef]
18. Valentini, F.; Roscioli, D.; Carbone, M.; Conte, V.; Floris, B.; Palleschi, G.; Flammini, R.; Bauer, E.M.; Nasillo, G.; Caponetti, E. Oxidized Graphene in Ionic Liquids for Assembling Chemically Modified Electrodes: A Structural and Electrochemical Characterization Study. *Anal. Chem.* **2012**, *84*, 5823–5831. [CrossRef]
19. Stankic, S.; Suman, S.; Haque, F.; Vidic, J. Pure and Multi Metal Oxide Nanoparticles: Synthesis, Antibacterial and Cytotoxic Properties. *J. Nanobiotechnol.* **2016**, *14*, 73. [CrossRef]
20. Valentini, F.; Roscioli, D.; Carbone, M.; Conte, V.; Floris, B.; Bauer, E.M.; Ditaranto, N.; Sabbatini, L.; Caponetti, E.; Chillura-Martino, D. Graphene and Ionic Liquids New Gel Paste Electrodes for Caffeic Acid Quantification. *Sens. Actuator B Chem.* **2015**, *212*, 248–255. [CrossRef]

21. Zhang, W.; Li, J.; Zhang, J.; Sheng, J.; He, T.; Tian, M.; Zhao, Y.; Xie, C.; Mai, L.; Mu, S. Top-Down Strategy to Synthesize Mesoporous Dual Carbon Armored MnO Nanoparticles for Lithium-Ion Battery Anodes. *ACS Appl. Mater. Interfaces* **2017**, *9*, 12680–12686. [CrossRef]
22. Casaletto, M.P.; Zanoni, R.; Carbone, M.; Piancastelli, M.N.; Aballe, L.; Weiss, K.; Horn, K. Ethylene Adsorption on Si(100)2 × 1: A High-resolution Photoemission Study. *Phys. Rev. B* **2000**, *62*, 17128–17133. [CrossRef]
23. Li, F.; Ran, J.; Jaroniec, M.; Qiao, S.Z. Solution Combustion Synthesis of Metal Oxide Nanomaterials for Energy Storage and Conversion. *Nanoscale* **2015**, *7*, 17590–17610. [CrossRef]
24. Carbone, M.; Caminiti, R. Adsorption States and Site Conversions of Phenylacetylene on Si(100)2 × 1 Calculated by DFT. *J. Theor. Comput. Chem.* **2012**, *11*, 1089–1099. [CrossRef]
25. Ortega, S.; Ibáñez, M.; Liu, Y.; Zhang, Y.; Kovalenko, M.V.; Cadavid, D.; Cabot, A. Bottom-up Engineering of Thermoelectric Nanomaterials and Devices from Solution-processed Nanoparticle Building Blocks. *Chem. Soc. Rev.* **2017**, *46*, 3510–3528. [CrossRef]
26. Carbone, M.; Piancastelli, M.N.; Casaletto, M.P.; Zanoni, R.; Besnard-Ramage, M.J.; Comtet, G.; Dujardin, G.; Hellner, L. Phenol Adsorption on Si (111)7 × 7 Studied by Synchrotron Radiation Photoemission and Photodesorption. *Surf. Sci.* **1999**, *419*, 114–119. [CrossRef]
27. de Oliveira, P.F.M.; Torresi, R.M.; Emmerling, F.; Camargo, P.H.C. Challenges and Opportunities in the Bottom-up Mechanochemical Synthesis of Noble Metal Nanoparticles. *J. Mater. Chem. A* **2020**, *8*, 16114–16141. [CrossRef]
28. Gontrani, L.; Tagliatesta, P.; Agresti, A.; Pescetelli, S.; Carbone, M. New Insights into the Structure of Glycols and Derivatives: A Comparative X-ray Diffraction, Raman and Molecular Dynamics Study of Ethane-1,2-diol, 2-methoxyethan-1-ol and 1,2-dimethoxy Ethane. *Crystals* **2020**, *10*, 1011. [CrossRef]
29. Mondal, K. Recent Advances in the Synthesis of Metal Oxide Nanofibers and Their Environmental Remediation Applications. *Inventions* **2017**, *2*, 9. [CrossRef]
30. Carbone, M. Cu-Zn-Co Nanosized Mixed Oxides Prepared from Hydroxycarbonate Precursors. *J. Alloys Compd.* **2016**, *688*, 202–209. [CrossRef]
31. Chen, Y.; Lu, W.; Guo, Y.; Zhu, Y.; Lu, H.; Song, Y. Synthesis, Characterization and Photocatalytic Activity of Nanocrystalline First Transition-Metal (Ti, Mn, Co, Ni and Zn) Oxisde Nanofibers by Electrospinning. *Appl. Sci.* **2019**, *9*, 8. [CrossRef]
32. Carbone, M.; Bauer, E.M.; Micheli, L.; Missori, M. NiO Morphology Dependent Optical and Electrochemical Properties. *Colloid Surf. A* **2017**, *532*, 178–182. [CrossRef]
33. Atchison, J.S.; Zeiger, M.; Tolosa, A.; Funke, L.M.; Jackel, N.; Presser, V. Electrospinning of Ultrafine Metal Oxide/Carbon and Metal Carbide/Carbon Nanocomposite Fibers. *RSC Adv.* **2015**, *5*, 35683–35692. [CrossRef]
34. Carbone, M.; Missori, M.; Micheli, L.; Tagliatesta, P.; Bauer, E.M. NiO Pseudocapacitance and Optical Properties: Does the Shape Win? *Materials* **2020**, *13*, 1417. [CrossRef] [PubMed]
35. Xia, X.; Zhang, Y.; Chao, D.; Guan, C.; Zhang, Y.; Li, L.; Ge, X.; Mínguez Bacho, I.; Tu, J.; Fan, H.J. Solution Synthesis of Metal Oxides for Electrochemical Energy Storage Applications. *Nanoscale* **2014**, *6*, 5008–5048. [CrossRef]
36. Djurišić, A.B.; Chen, X.; Leung, Y.H.; Ching Ng, A.M. ZnO Nanostructures: Growth, Properties and Applications. *J. Mater. Chem.* **2012**, *22*, 6526–6535. [CrossRef]
37. Wang, J.; Chen, R.; Xiang, L.; Komarneni, S. Synthesis, Properties and Applications of ZnO Nanomaterials with Oxygen Vacancies: A review. *Ceram. Int.* **2018**, *44*, 7357–7377. [CrossRef]
38. Son, D.-Y.; Im, J.-H.; Kim, H.-S.; Park, N.-G. Efficient Perovskite Solar Cell Based on ZnO Nanorods: An Effective Charge Collection System. *J. Phys. Chem. C* **2014**, *118*, 16567–16573. [CrossRef]
39. Wang, X.; Sun, F.; Duan, Y.; Yin, Z.; Luo, W.; Huang, Y.; Chen, J. Highly Sensitive, Temperature-dependent Gas Sensor Based on Hierarchical ZnO Nanorod Arrays. *J. Mater. Chem. C* **2015**, *3*, 11397–11405. [CrossRef]
40. Lee, K.M.; Lai, C.W.; Ngai, K.S.; Juan, J.C. Recent Developments of Zinc Oxide Based Photocatalyst in Water Treatment Technology: A Review. *Water Res.* **2016**, *88*, 428–448. [CrossRef]
41. He, Y.-B.; Li, G.-R.; Wang, Z.-L.; Su, C.-Y.; Tong, Y.-X. Single-crystal ZnO Nanorod/Amorphous and Nanoporous Metal Oxide Shell Composites: Controllable Electrochemical Synthesis and Enhanced Supercapacitor Performances. *Energy Environ. Sci.* **2011**, *4*, 1288–1292. [CrossRef]
42. Ong, C.B.; Ng, L.Y.; Mohammad, A.W. A Review of ZnO Nanoparticles as Solar Photocatalysts: Synthesis, Mechanisms and Applications. *Renew. Sustain. Energy Rev.* **2018**, *81*, 536–551. [CrossRef]
43. Ammar, S.H.; Abdulnabi, W.A.; Abdul Kader, H.D. Synthesis, Characterization and Environmental Remediation Applications of Polyoxometalates-based Magnetic Zinc Oxide Nanocomposites (Fe_3O_4@ZnO/PMOs). *Environ. Nanotechnol. Monit. Manag.* **2020**, *13*, 100289. [CrossRef]
44. Donia, D.T.; Carbone, M. Fate of the Nanoparticles in Environmental Cycles. *Int. J. Environ. Sci. Technol.* **2019**, *16*, 583–600. [CrossRef]
45. Carbone, M.; Briancesco, R.; Bonadonna, L. Antimicrobial Power of Cu/Zn Mixed Oxide Nanoparticles to *Escherichia coli*. *Environ. Nanotechnol. Monit. Manag.* **2017**, *7*, 97–102. [CrossRef]
46. Sheoran, P.; Grewal, S.; Kumari, S.; Goel, S. Enhancement of Growth and Yield, Leaching Reduction in *Triticum aestivum* Using Biogenic Synthesized Zinc Oxide Fertilizer. *Biocatal. Agric. Biotechnol.* **2021**, *32*, 101938. [CrossRef]

47. Oliveira, A.P.A.; Hochepied, J.-F.; Grillon, F.; Berger, M.-H. Controlled Precipitation of Zinc Oxide Particles at Room Temperature. *Chem. Mater.* **2003**, *15*, 3202–3207. [CrossRef]
48. Cao, H.L.; Qian, X.F.; Gong, Q.; Du, W.M.; Ma, X.D.; Zhu, Z.K. Shape- and Size-controlled Synthesis of Nanometre ZnO from a Simple Solution Route at Room Temperature. *Nanotechnology* **2006**, *17*, 3632–3636. [CrossRef]
49. Stahl, R.; Jung, C.; Lutz, H.D.; Kockelmann, W.; Jacobs, H. Kristallstrukturen und Wasserstoffbrückenbindungen bei β-$Be(OH)_2$ und ϵ-$Zn(OH)_2$. *Z. Anorg. Allg. Chem.* **1998**, *624*, 1130–1136. [CrossRef]
50. Wang, M.; Zhang, Y.; Zhou, Y.; Yang, F.; Kim, E.J.; Hahn, S.H.; Seong, S.G. Rapid Room-temperature Synthesis of Nanosheet Assembled ZnO Mesocrystals with Excellent Photocatalytic Activity. *CrystEngComm* **2013**, *15*, 754–763. [CrossRef]
51. Wahab, R.; Ansari, S.G.; Kim, Y.-S.; Seo, H.-K.; Shin, H.-S. Room Temperature Synthesis of Needle-shaped ZnO Nanorods via Sonochemical Method. *App. Surf. Sci.* **2007**, *253*, 7622–7626. [CrossRef]
52. Jaber, B.; Laânab, L. One Step Synthesis of ZnO Nanoparticles in Free Organic Medium: Structural and Optical Characterizations. *Mater. Sci. Semicon. Proc.* **2014**, *27*, 446–451. [CrossRef]
53. Li, S.-M.; Zhang, L.-X.; Zhu, M.-Y.; Ji, G.-J.; Zhao, L.-X.; Yin, J.; Bie, L.-J. Acetone Sensing of ZnO Nanosheets Synthesized Using Room-temperature Precipitation. *Sens. Actuator B Chem.* **2017**, *249*, 611–623. [CrossRef]
54. Kumar, V.R.; Wariar, P.R.S.; Prasad, V.S.; Koshy, J. A Novel Approach for the Synthesis of Nanocrystalline Zinc Oxide Powders by Room Temperature Co-precipitation Method. *Mater. Lett.* **2011**, *65*, 2059–2061. [CrossRef]
55. Liu, Y.; Gao, W. Growth Process, Crystal Size and Alignment of ZnO Nanorods Synthesized under Neutral and Acid Conditions. *J. Alloys Compd.* **2015**, *629*, 84–91. [CrossRef]
56. Toby, B.H.; Von Dreele, R.B. GSAS-II: The Genesis of a Modern Open-source All Purpose Crystallography Software Package. *J. Appl. Cryst.* **2013**, *46*, 544–549. [CrossRef]
57. Xu, Y.N.; Ching, W.Y. Electronic, Optical, and Structural Properties of Some Wurtzite Crystals. *Phys. Rev. B* **1993**, *48*, 4335–4351. [CrossRef]
58. Downs, R.T.; Hall-Wallace, M. The American Mineralogist Crystal Structure Database. *Am. Mineral.* **2003**, *88*, 247–250.
59. Finger, L.W.; Cox, D.E.; Jephcoat, A.P. A Correction for Powder Diffraction Peak Asymmetry Due to Axial Divergence. *J. Appl. Cryst.* **1994**, *27*, 892–900. [CrossRef]
60. Warren, B.E. *X-ray Diffraction*; Dover Publications, Inc.: New York, NY, USA, 1990.
61. Campetella, M.; Mariani, A.; Sadun, C.; Wu, B.; Castner, E.W., Jr.; Gontrani, L. Structure and Dynamics of Propylammonium Nitrate-acetonitrile Mixtures: An Intricate Multi-scale System Probed with Experimental and Theoretical Techniques. *J. Chem. Phys.* **2018**, *148*, 134507. [CrossRef]
62. Haynes, W.M. (Ed.) *CRC Handbook of Chemistry and Physics*, 94th ed.; CRC Press: Boca Raton, FL, USA, 2014; pp. 4–100.
63. Kubelka, P.; Munk, F. Ein Beitrag Zur Optik Der Farbanstriche. *Z. Tech. Phys.* **1931**, *12*, 593–601.
64. Missori, M.; Pulci, O.; Teodonio, L.; Violante, C.; Kupchak, I.; Bagniuk, J.; Łojewska, J.; Mosca Conte, A. Optical Response of Strongly Absorbing Inhomogeneous Materials: Application to paper degradation. *Phys. Rev. B* **2014**, *89*, 054201. [CrossRef]
65. Missori, M. Optical Spectroscopy of Ancient Paper and Textiles. *Nuovo Cim. C* **2016**, *39*, 293.
66. Smith, R.A. *Semiconductors*, 2nd ed.; Cambridge University Press: Cambridge, UK, 1978.
67. Brus, L.E. Electron-electron and Electron-hole Interactions in Small Semiconductor Crystallites: The Size Dependence of the Lowest Excited Electronic State. *J. Chem. Phys.* **1984**, *80*, 4403–4409. [CrossRef]
68. Sayari, A. Characterization of Nanocrystalline ZnO Flakes Synthesized by a Simple Reaction Process. *KONA Powder Part. J.* **2013**, *30*, 119–124. [CrossRef]
69. Repp, S.; Erdem, E. Controlling the Exciton Energy of Zinc Oxide (ZnO) Quantum Dots by Changing the Confinement Conditions. *Spectrochim. Acta A* **2016**, *152*, 637–644. [CrossRef]
70. Studenikin, S.A.; Golego, N.; Cocivera, M. Fabrication of Green and Orange Photoluminescent, Undoped ZnO Films Using Spray Pyrolysis. *J. Appl. Phys.* **1998**, *84*, 2287. [CrossRef]
71. Debanath, M.K.; Karmakar, S. Study of Blue Shift of Optical Band Gap in Zinc Oxide (ZnO) Nanoparticles Prepared by Low-temperature Wet Chemical Method. *Mater. Lett.* **2013**, *111*, 116–119. [CrossRef]
72. Lin, K.-F.; Cheng, H.-M.; Hsu, H.-C.; Lin, L.-J.; Hsieh, W.-F. Band Gap Variation of Size-controlled ZnO Quantum Dots Synthesized by Sol–gel Method. *Chem. Phys. Lett.* **2005**, *409*, 208–211. [CrossRef]
73. Davis, K.; Yarbrough, R.; Froeschle, M.; White, J.; Rathnayake, H. Band Gap Engineered Zinc Oxide Nanostructures via a Sol–gel Synthesis of Solvent Driven Shapecontrolled Crystal Growth. *RSC Adv.* **2019**, *9*, 14638–14648. [CrossRef]